Hopping of the center-of-mass of single G centers in silicon-on-insulator

Alrik Durand, Yoann Baron, Péter Udvarhelyi, Félix Cache, Krithika V R., Tobias Herzig, Mario Khoury, Sébastien Pezzagna, Jan Meijer, Jean-Michel Hartmann, et al.

▶ To cite this version:

Alrik Durand, Yoann Baron, Péter Udvarhelyi, Félix Cache, Krithika V R., et al.. Hopping of the center-of-mass of single G centers in silicon-on-insulator. Phys.Rev.X, 2024, 14 (4), pp.041071. ⟨10.1103/PhysRevX.14.041071⟩. ⟨hal-04600016⟩

HAL Id: hal-04600016

https://hal.science/hal-04600016v1

Submitted on 27 Feb 2025

PHYSICAL REVIEW X **14,** 041071 (2024)

Hopping of the Center-of-Mass of Single G Centers in Silicon-on-Insulator

Alrik Durand,[1,*] Yoann Baron,[1,*] Péter Udvarhelyi,[2,3] Félix Cache,[1] Krithika V. R.,[1] Tobias Herzig,[4]
Mario Khoury,[5] Sébastien Pezzagna,[4] Jan Meijer,[4] Jean-Michel Hartmann,[6] Shay Reboh,[6]
Marco Abbarchi,[5,7] Isabelle Robert-Philip,[1] Adam Gali,[2,3,8] Jean-Michel Gérard,[9]
Vincent Jacques,[1] Guillaume Cassabois,[1,10] and Anaïs Dréau[1,†]

[1] *Laboratoire Charles Coulomb, Université de Montpellier and CNRS, 34095 Montpellier, France*
[2] *HUN-REN Wigner Research Centre for Physics, P.O. Box 49, H-1525 Budapest, Hungary*
[3] *Department of Atomic Physics, Institute of Physics, Budapest University of Technology and Economics,*
Műegyetem rakpart 3, H-1111 Budapest, Hungary
[4] *Division of Applied Quantum Systems, Felix-Bloch Institute for Solid-State Physics, University Leipzig,*
Linnéestraße 5, 04103 Leipzig, Germany
[5] *CNRS, Aix-Marseille Université, Centrale Marseille, IM2NP,*
UMR 7334, Campus de St. Jérôme, 13397 Marseille, France
[6] *Université Grenoble Alpes, CEA, LETI, F-38000 Grenoble, France*
[7] *Solnil, 95 Rue de la République, 13002 Marseille, France*
[8] *MTA-WFK Lendület "Momentum" Semiconductor Nanostructures Research Group, Budapest, Hungary*
[9] *Université Grenoble Alpes, CEA, Grenoble INP, IRIG, PHELIQS, 38000 Grenoble, France*
[10] *Institut Universitaire de France, 75231 Paris, France*

(Received 23 April 2024; revised 23 July 2024; accepted 28 October 2024; published 27 December 2024)

Among the wealth of single fluorescent defects recently detected in silicon, the G center catches interest for its telecom single-photon emission that could be coupled to a metastable electron spin triplet. The G center is a unique defect where the standard Born-Oppenheimer approximation used in solid-state physics breaks down as one of its atoms, a silicon atom in interstitial position $\mathrm{Si}_{(\mathrm{i})}$, can move between six sites. The impact of its displacement, due either to coherent tunneling or to random jumps from one site to another, on the optical properties of G centers is still largely unknown, especially in silicon-on-insulator (SOI) samples. Here, we investigate the displacement of the center of mass of the G center in silicon. By performing photoluminescence experiments at single-defect scale, we show that individual G defects in SOI exhibit several emission dipoles and zero-phonon line fine structures with splittings up to approximately 1 meV, both indicating a motion of the defect central atom over time. Combining polarization and spectral analysis at the single-photon level, we evidence that the reconfiguration dynamics is drastically different from the one of the unperturbed G center in bulk silicon where the mobile atom is fully delocalized over all six sites through tunneling. The SOI structure freezes the $\mathrm{Si}_{(\mathrm{i})}$ delocalization of the G defect and, as a result, enables one to isolate linearly polarized optical lines. Under above-band-gap optical excitation, the central atom of G centers in SOI behaves as if it were in a six-slot roulette wheel, randomly alternating between localized crystal sites at each optical cycle. Comparative measurements in a bulk silicon sample and *ab initio* calculations highlight that strain is likely the dominant perturbation impacting the G center geometry. These results shed light on the importance of the atomic reconfiguration dynamics to understand and control the photoluminescence properties of the G center in silicon. More generally, these findings emphasize the impact of strain fluctuations inherent to SOI wafers for future quantum integrated photonics applications based on color centers in silicon.

DOI: 10.1103/PhysRevX.14.041071

Subject Areas: Condensed Matter Physics, Optics, Quantum Physics

I. INTRODUCTION

Color centers in silicon have recently received renewed attention, as they could offer a new building block for quantum technologies [1–33]. Within a few years, single-photon emission has been demonstrated on a dozen of different types of fluorescent defects in silicon [3,5,7,9,16,17,23,28,31]. One of the next challenges is to

---

[*] These authors contributed equally to this work.

[†] Contact author: anais.dreau@umontpellier.fr

provide single spin qubits interfaced with telecom light and integrated into silicon-on-insulator (SOI) photonic nanostructures [9]. Therefore, strong emphasis has been placed on color centers with nonzero electron spin that could be optically initialized and read out, such as the *T* center [8–14], dopants [26–28], or the G center [1,2,15–22,24,34]. This last defect is the brightest among the three, and it can be isolated at single-defect scale in unstructured SOI wafers [16].

The G center in silicon is a fluorescent carbon-based complex studied for several decades [35–37] and commonly used as a nondestructive probe of the carbon concentration [38]. Besides an optical emission in the telecom *O* band, the G center features a metastable electron spin triplet whose magnetic resonances have been measured optically on ensembles [34,39]. Single isolated G centers can be created by coimplantation of carbon ions and protons [16] or by Si-focused ion beam implantation in carbon-implanted silicon with a spatial resolution of 50 nm [17]. Purcell-enhanced emission has recently been demonstrated for ensembles of G centers [19] and single G centers [21] in a photonic cavity, as well as Hong-Ou-Mandel interferences using an individual G defect integrated in a silicon waveguide [18].

Despite these advances, our knowledge on the photophysics of the G center in silicon remains limited. Unlike usual solid-state systems, this defect cannot be described under the standard Born-Oppenheimer approximation used in solid-state physics, since its atomic structure is not fixed. One of its constitutive atoms is not rigidly bound and can occupy six different sites [15,34,37,38,40], corresponding to radically different atomic configurations and positions of the defect center of mass. How this structural reconfiguration impacts the optical properties of the G center in SOI is very little known, which hinders the development of potential quantum applications.

In this work, we explore the motion of the center of mass of the G center in silicon. We start by introducing the atomic configuration of the unperturbed defect and the energy-level fine structure resulting from the rotational delocalization through tunneling of its mobile atom. Single G centers in SOI are then investigated through low-temperature photoluminescence (PL) experiments. Their single-photon polarization is first analyzed to reveal that the G center emission is associated to several dipole orientations. We then examine the zero-phonon line spectra of these individual defects and show a fine structure with line splittings exceeding by 2 orders of magnitude the ones of unperturbed G centers. By combining spectral and polarization analysis, we demonstrate that the center of mass of these G centers is hopping over time between localized positions, like a ball in a six-slot roulette wheel. Finally, performing spectral measurements in a bulk silicon sample enables one to evidence strain effects as the dominant perturbation freezing the rotational delocalization of single G centers in SOI structures. Our experimental results are interpreted by means of symmetry point group theory analysis and density functional theory calculations for understanding the structural and electronic properties of the G centers, complemented by finite-difference time-domain simulations for the polarization emission diagrams of G centers in SOI. In conclusion, we discuss the impact of these findings on the control of the quantum properties of single G centers in SOI platforms.

II. UNPERTURBED G CENTER IN SILICON

The microscopic structure of the luminescent form of the G center in silicon was proposed in the 1980s [37,39,41] and recently confirmed by advanced *ab initio* calculations [15]. This atomic configuration is displayed in Fig. 1(a). It consists of two substitutional carbon atoms aligned along the $\langle 111 \rangle$ crystal direction and connected by an interstitial silicon atom $\mathrm{Si}_{(\mathrm{i})}$. This defect configuration corresponds to a C_{1h} symmetry, with a plane of symmetry defined by these three atoms [15]. Unlike the tetravalent carbon atoms, the $\mathrm{Si}_{(\mathrm{i})}$ forms only two covalent bonds with its neighboring atoms and is, therefore, less rigidly attached to the matrix. Indeed, recent density functional theory (DFT) simulations have shown that this silicon atom does rotate around the C-C axis [15]. More precisely, in both ground and excited states, the interstitial silicon atom is delocalized by tunnel effect between the six equivalent sites indicated in Fig. 1(b) [15].

Because of the displacement of its center of mass linked to the $\mathrm{Si}_{(\mathrm{i})}$ motion, the standard Born-Oppenheimer approximation used in solid-state physics breaks down for the G center in silicon. In other terms, the $\mathrm{Si}_{(\mathrm{i})}$ nucleus position cannot be considered as frozen at a fixed site when solving the electronic wave functions and energies of the defect. Nevertheless, this rotational degree of freedom can be introduced in a simple tight-binding model to extract the defect eigenstates and associated energies, as proposed in Ref. [15]. As in the first step of the standard Born-Oppenheimer approximation, the electronic wave function of the G defect can be written as the product of its center-of-mass wave function $\varphi(\boldsymbol{R}_{\mathrm{c.m.}})$ by the wave function of the electron cloud relative to the center of mass $\phi(\boldsymbol{r}-\boldsymbol{R}_{\mathrm{c.m.}})$:

$$\psi(\boldsymbol{r}) = \varphi(\boldsymbol{R}_{\mathrm{c.m.}}) \cdot \phi(\boldsymbol{r}-\boldsymbol{R}_{\mathrm{c.m.}}). \tag{1}$$

This expression holds in both ground and excited states, but, to simplify notations, we omit the indices GS and ES referring to the ground and excited states, respectively. As the electron cloud reconfiguration is several orders of magnitude faster, it always follows adiabatically the motion of the defect center of mass. The DFT-calculated potential energy surface (PES) along the motion path of the $\mathrm{Si}_{(\mathrm{i})}$ can be approximated by a six-period cosine function in both ground and excited states, albeit with different barrier

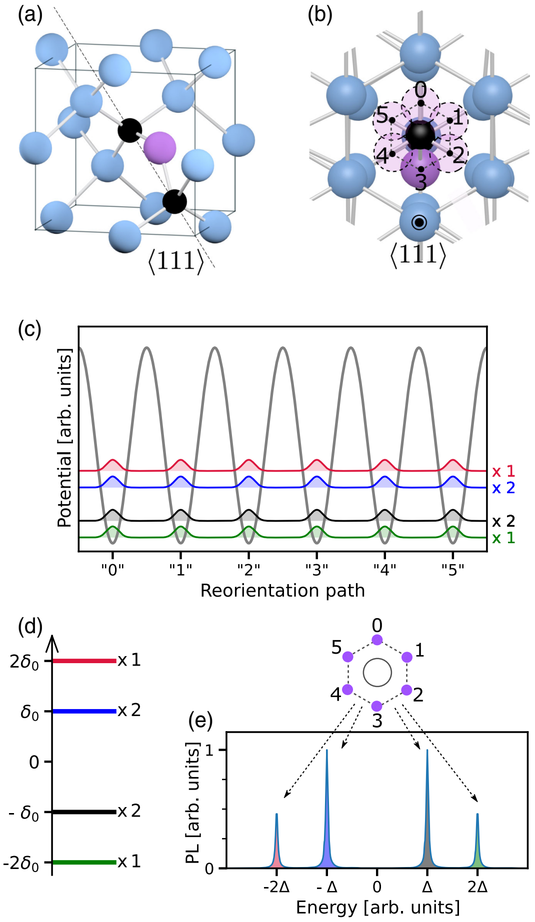

FIG. 1. The G center in silicon in the unperturbed case. (a) Microscopic structure of the defect. Two substitutional carbon atoms C (black) connected by an interstitial silicon atom $\mathrm{Si}_{(\mathrm{i})}$ (purple) are aligned along the $\langle 111\rangle$ crystal axis. (b) In the $\langle 111\rangle$ direction, the G center structure showing the six possible equivalent sites for the $\mathrm{Si}_{(\mathrm{i})}$. (c) In gray, a sketch of the energy potential of the six identical coupled wells experienced by the $\mathrm{Si}_{(\mathrm{i})}$ along its motion path around the C-C axis. This potential is similar in both the electronic ground and excited states of the G center, albeit with different barrier heights [15]. In colors, density distributions for the six rotational states of the defect center of mass, with level degeneracy indicated on the right. The rotational energy splittings are shifted for clarity and should not be compared to the potential barrier energy. (d) Quartet energy-level structure of the six delocalized states of the center of mass of the G center. Energies are offset by E_0 (see the main text). (e) Theoretical zero-phonon line spectrum of the unperturbed G center in both absorption and photoluminescence. Δ is the difference between the quartet energy splittings in the ground and excited states. Each emission line corresponds to optical transitions between rotational states where the $\mathrm{Si}_{(\mathrm{i})}$ is equally delocalized over the six sites.

amplitudes [15]. Because of the tunnel coupling between adjacent sites, the silicon atom, thus, behaves like a quasiparticle in a potential of six identical coupled wells [Fig. 1(c)]. Using the Bloch theorem, the six rotational eigenstates of the defect center of mass can be expressed in Dirac notation as

$$|\varphi^{(m)}\rangle = \frac{1}{\sqrt{6}}\sum_{n=0}^{5} e^{ik_m na}|n\rangle, \tag{2}$$

where $m \in [\![0,5]\!]$, k_m is the wave vector of the Bloch function, a is the period of the potential, and $|n\rangle$ is the wave function describing the $\mathrm{Si}_{(\mathrm{i})}$ atom localized in the site n. From this equation, we directly get that the $\mathrm{Si}_{(\mathrm{i})}$ is equally delocalized on the six possible sites for each eigenstate of the G center [Fig. 1(c)]. In other terms, the probability to measure it in any of the positions shown in Fig. 1(b) is $1/6$. However, as a result of its delocalization, the $\mathrm{Si}_{(\mathrm{i})}$ average position, and, therefore, the defect center of mass, is on the $\langle 111\rangle$ axis for all six stationary rotational states. The wave vector expression is derived from the Born–von Karman boundary conditions ($e^{ik_m 6a} = 1$):

$$k_m = \frac{m\pi}{3a}. \tag{3}$$

The time-independent Schrödinger equation describing the stationary states of the defect center of mass is $\mathcal{H}|\varphi^{(m)}\rangle = E^{(m)}|\varphi^{(m)}\rangle$. Considering $E_0 = \langle n|\mathcal{H}|n\rangle$ the energy of each uncoupled site and $\delta_0 = \langle n|\mathcal{H}|n \pm 1\rangle$ the tunneling coupling energy between adjacent sites, the energy of the eigenstate $|\varphi^{(m)}\rangle$ is written as

$$E^{(m)} = E_0 + 2\delta_0 \cos(k_m a). \tag{4}$$

Combining Eqs. (4) and (3), we finally obtain the formula for the six eigenenergies of the defect center of mass:

$$E^{(m)} = E_0 + 2\delta_0 \cos\left(m\frac{\pi}{3}\right). \tag{5}$$

The rotational energy levels of the G center, in both ground and excited states, are, thus, arranged in a quartet fine structure with degeneracy 1:2:2:1 and splittings δ_0-$2\delta_0$-δ_0, as represented in Fig. 1(d). However, due to a higher energy barrier for the $\mathrm{Si}_{(\mathrm{i})}$ rotation, the tunneling coupling energy is much smaller in the ground state [15]. As a result, the quartet energy splitting in this level is negligible compared to the excited one: $\delta_{0,\mathrm{GS}} \ll \delta_{0,\mathrm{ES}}$. We note that the same quartet structure is found for the electronic states of the benzene molecule [15]. Indeed, the G center in silicon and the benzene molecule share similar electronic wave functions resulting from the delocalization of their components in a six-well periodic potential. For the benzene, the electrons are delocalized in the potential created by six fixed nuclei, whereas for the G center, it is the $\mathrm{Si}_{(\mathrm{i})}$ that is delocalized between six crystal sites and instantaneously followed by the electron cloud.

In the Franck-Condon approximation, the selection rules for optical dipolar transitions between these levels are given by

$$\langle\psi_{\mathrm{GS}}|-\boldsymbol{d}\cdot\boldsymbol{E}|\psi_{\mathrm{ES}}\rangle = \langle\varphi_{\mathrm{GS}}^{(m)}|\varphi_{\mathrm{ES}}^{(m')}\rangle\cdot\langle\phi_{\mathrm{GS}}|-\boldsymbol{d}\cdot\boldsymbol{E}|\phi_{\mathrm{ES}}\rangle. \qquad (6)$$

Since $\langle\varphi_{\mathrm{GS}}^{(m)}|\varphi_{\mathrm{ES}}^{(m')}\rangle = \delta_{m,m'}$ the Kronecker symbol, the rotational quantum number m must be preserved during the optical transition. Hence, optical transitions are allowed only between the same rotational eigenstates. Let Δ be the difference between the tunneling coupling energy in the ground and excited states: $\Delta = |\delta_{0,_{\mathrm{ES}}} - \delta_{0,_{\mathrm{GS}}}|$. From the optical selection rules, it results that a quartet fine structure with relative line intensities 1:2:2:1 and splittings Δ-2Δ-Δ should be observed in absorption and emission [Fig. 1(e)]. Indeed, such quartet spectra have been measured on an ensemble of G centers in isotopically purified bulk ^{28}Si [2]. In both absorption and PL spectra, the energy splitting is $\Delta^{(\mathrm{exp})} = 2.5 \pm 0.2$ μeV (0.60 ± 0.05 GHz). As previously mentioned, since $\Delta \simeq \delta_{0,_{\mathrm{ES}}}$, the average time for the Si$_{(\mathrm{i})}$ atom to tunnel from one site to another in the excited state can be approximated by $t_0 \simeq \pi\hbar/(2\Delta)$ [42]. By using the experimental splitting value $\Delta^{(\mathrm{exp})}$ from Ref. [2], we obtain $t_0 \simeq 0.41$ ns. Concerning G centers at the single-defect scale, neither this quartet structure nor any other fine structure has been reported so far.

III. SINGLE G CENTERS IN SOI

The silicon sample used here is the SOI wafer from Ref. [16]. Its top silicon layer is made of 54 nm of isotopically pure ^{28}Si grown at 650 °C, 20 Torr with ^{28}SiH$_4$ in a reduced pressure-chemical vapor deposition reactor, on top of 4 nm of silicon with natural isotope abundance. To create G centers, it is locally coimplanted with carbon ions and protons at 8 and 6 keV energies, respectively, using several fluences $\geq 3\times10^{10}$ cm^{-2} [16]. The experimental setup is a homemade confocal microscope built in a He-closed cycle cryostat, equipped with superconducting single-photon detectors (more details in Refs. [3,24]). We perform above-band-gap optical excitation using a 532-nm continuous laser and select sample areas in which well-separated single G centers can be optically addressed. For practical reasons, all measurements have been performed at 30 K.

Optical raster scans of the SOI silicon sample with ^{28}Si on top show well-isolated light spots [Fig. 2(a)]. Their PL spectra enable an unambiguous identification of genuine G centers due to the presence of a zero-phonon line (ZPL) at 1278 nm and the E line at 1382 nm [Fig. 2(b)] [24]. The single-photon emission is confirmed by the observation of antibunching at zero delay in the autocorrelation function $g^{(2)}(\tau)$ of the PL signal [Fig. 2(c)].

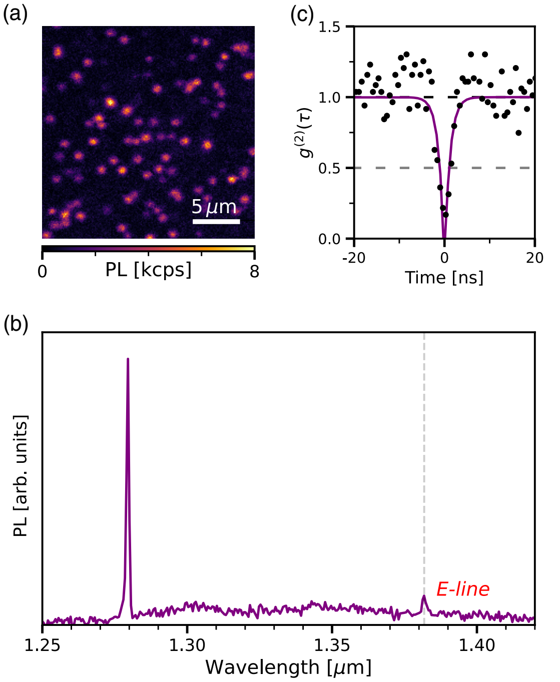

FIG. 2. The G center in silicon. (a) Optical scan at 30 K of the SOI sample coimplanted with carbon ions and protons [16]. Hot spots are isolated G centers. (b) Low-resolution PL spectrum of a single G center showing the zero-phonon line at 1279 nm and the E line associated with the defect local-vibrational mode. (c) Second-order autocorrelation function demonstrating single-photon emission with an antibunching at zero delay $g^{(2)}(0) \simeq 0.17 < 1/2$.

IV. ANALYSIS OF THE SINGLE-PHOTON POLARIZATION

A. Measurements

Analysis of the polarization of single photons from G centers reveals a luminescence mechanism more complex than an optical transition associated with a single-emission dipole orientation. Emission polarization diagrams are acquired on single G defects by rotating a half-wave plate in front of a fixed polarizer in the detection path. PL photons are collected perpendicularly to the (001) top surface of the ^{28}SOI sample. To retain only the G center PL, diagrams are corrected from unpolarized background contribution measured at a single point close to defects. The first observation from Figs. 3(a) and 3(b) is that the polarization emission diagrams of single G centers are strongly anisotropic. For some G defects, the PL signal is maximum at 90°, corresponding to the crystal axis $[1\bar{1}0]$ [Fig. 3(a)]. In contrast, for others, a PL maximum is detected at 0°, i.e., toward the [110] axis [Fig. 3(b)]. A statistical analysis of 39G centers in ^{28}SOI shows that only these two directions are permitted, with 50/50 probability within statistical fluctuations [Fig. 3(c)]. Another information from these diagrams is that no half-wave plate angle can cancel the PL signal from single G centers, as all diagrams show a visibility $\leq 68\%$ [Fig. 3(d)]. The average

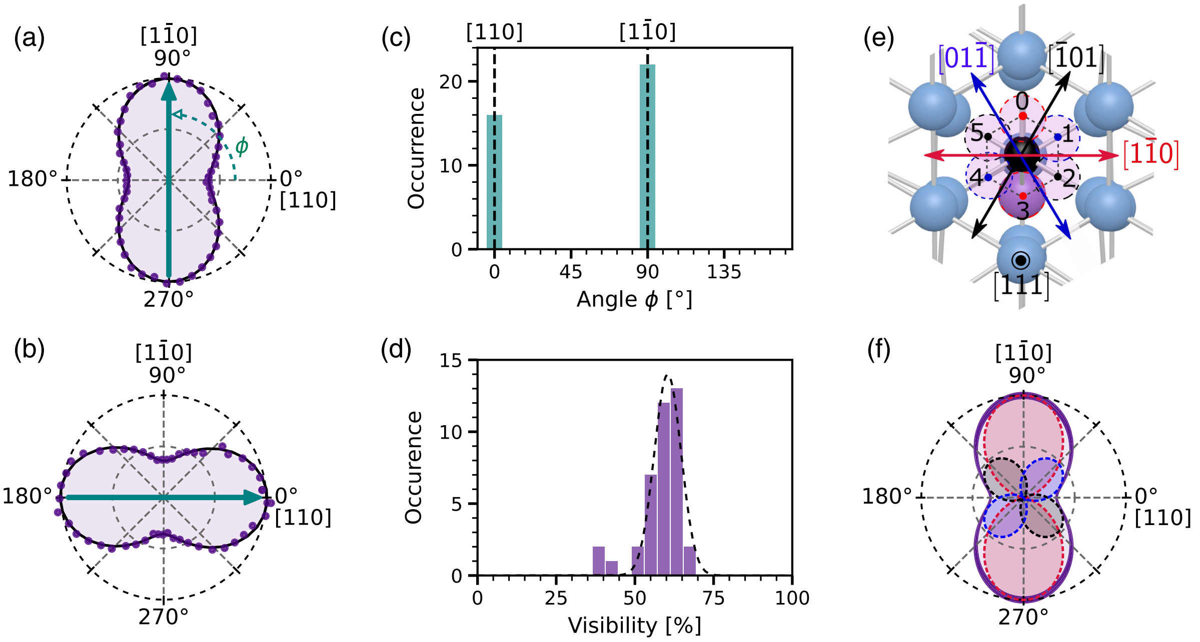

FIG. 3. Polarization emission diagrams of single G centers in silicon. (a),(b) Typical polarization emission diagrams recorded on two single G centers and corrected from background counts (see the main text). The diagram visibility V and orientation angle ϕ are extracted from data fitting (solid lines) with a function $V \cdot \cos^2(\theta - \phi) + 1 - V$. Note that θ is the angle of the detected polarization, i.e., twice the angle of the rotating half-wave plate. (c),(d) Histograms of the distribution of the angle ϕ and visibility V measured on 39 G centers, respectively. (e) Orientations of the emission dipoles of a [111]-oriented G center depending on the position of the $\mathrm{Si}_{(\mathrm{i})}$: dipoles along $[1\bar{1}0]$, $[01\bar{1}]$, and $[\bar{1}01]$ for the $\mathrm{Si}_{(i)}$ positions $\{0, 3\}$, $\{1, 4\}$, and $\{2, 5\}$, respectively. (f) Polarization emission diagrams (dashed lines) for each of the three dipoles considering photon collection from the (001)-top surface. Their amplitudes correspond to the relative ratio of PL collected intensity (see the main text). The indigo thick line represents the total polarization diagram resulting from the contribution of the three dipoles (Appendix A).

visibility over the set is 58%, with a standard deviation of 7%. The polarization diagrams of single G centers cannot be explained by the presence of a single-emission dipole. As a consequence, the G center luminescence originates from multiple dipoles.

B. Interpretation

To understand the polarization emission diagram of the G center, we need to return to its microscopic structure. The interstitial silicon atom can take six positions in the plane perpendicular to the $\langle 111 \rangle$ defect main axis, as shown in Fig. 1(b). For a given static position of $\mathrm{Si}_{(i)}$, symmetry point group theory for C_{1h} symmetry authorizes a single-emission dipole perpendicular to the symmetry plane [15]. For a [111]-oriented G center, this leads to three pairs of possible dipoles aligned along the $[1\bar{1}0]$, $[01\bar{1}]$, and $[\bar{1}01]$ axes for the $\{0, 3\}$, $\{1, 4\}$, and $\{2, 5\}$ $\mathrm{Si}_{(i)}$ positions, respectively [Fig. 3(e)]. From simple symmetry considerations, when projected onto the (001) sample top surface from which PL is collected at normal incidence, these dipoles produce linearly polarized photons at 90°, 45°, and 135°, respectively. The three corresponding polarization diagrams are, therefore, oriented along these angles, each with a visibility of 100%. None of these dipoles taken alone can explain the single-photon polarization observed from individual G centers [see Figs. 3(a)–3(d)]. The far field emission diagram of each of these three dipoles collected within the numerical aperture of our microscope objective can be simulated using the finite-difference time-domain (FDTD) method [43]. These calculations show that the PL collected for the $[1\bar{1}0]$ dipole, that is parallel to the (001) top surface, is between 2.03 and 2.17 times more intense than that of the other two dipoles, depending on the defect depth in the Si layer (Appendix A). Considering these three emission dipoles as independent and equally probable, we obtain the polarization diagram in Fig. 3(f), pointing toward $[1\bar{1}0]$ and with a visibility varying between 67.0% and 68.5% depending on depth. The same polarization diagram would also be obtained for a $[\bar{1}\bar{1}1]$-oriented G center, while G centers aligned along $[\bar{1}11]$ or $[1\bar{1}1]$ would give diagrams turned by 90°. This model is in very good agreement with the experimental data in Figs. 3(a)–3(d), allowing one to conclude that the interstitial silicon atom of these single G centers does move over time during the measurements. Note that, at this stage, it is not possible to deduce whether or not these G defects are in the unperturbed geometry described in Sec. II. Since the electron density is equally distributed over the six sites for all energy levels, each of the three dipoles has the same probability to emit and the polarization diagram should be identical to the one from Fig. 3(f). To gain more information about their center-of-mass motion, we need to examine the fine structure of these individual G centers.

V. ZPL FINE STRUCTURE

A. Measurements

High-resolution PL spectra recorded on individual G defects show a fine structure radically different from the one presented in Fig. 1(e). Figure 4(a) displays the ZPL spectra recorded on seven individual G centers in ^{28}SOI for which antibunching with $g^{(2)}(0) < 1/2$ has been measured with no spectral filtering. Except for one defect (G-5), all G centers show at least two or three ZPL lines. Since single defects are investigated here, these multiple lines are evidence of a fine structure of the G center. This effect is to be distinguished from a lifting of orientational degeneracy under stress between nonequivalent defect orientations in ensembles of G centers [35,44,45]. These fine structures cannot be explained by a static configuration with no $\mathrm{Si}_{(\mathrm{i})}$ displacement, as the associated C_{1h} monoclinic point group symmetry would allow only a single transition between A' and A'' singlet orbital levels [15]. The disparity in pattern and line positions observed between defects indicates an extrinsic origin, resulting from different local environments. Importantly, the quartet fine structure reported on unperturbed G centers has a characteristic splitting of 10 μeV, more than 2 orders of magnitude smaller than in Fig. 4(a) [2]. Because of the spectral resolution of our spectrometer (≃150 μeV), such a quartet would appear as a single-emission line in the spectra. The fine structures with meV-line splittings in Fig. 4(a) rather indicate a significant perturbation of single G centers induced by their local environment.

PL spectra of individual G centers in SOI strongly change with polarization filtering. We focus on the single G-0 and G-1 defects that both have well-resolved fine structures. The G-0 center shows a doublet fine structure with an energy separation of 0.70 ± 0.02 meV. As shown in Fig. 4(b), when the detected polarization is perpendicular to the main axis of the defect emission diagram, the highest-energy line L_0 is completely extinguished. When the selected polarization is parallel, the L_0 line is similar to the previous spectrum with no polarization filtering. On the contrary, the second line L_1 has the same intensity for both polarization angles, corresponding to roughly one-half compared to the unfiltered spectrum. A similar behavior is observed on the triplet fine structure of the G-1 defect whose splittings from L_0 to L_2 are 1.00 ± 0.02 and 0.86 ± 0.02 meV [Fig. 4(c)]. The strongest line L_0 is globally unchanged for the polarization parallel to the orientation of the G-1 diagram and cancels out for the perpendicular orientation. The intensity of the other two lines L_1 and L_2 is roughly decreased by a factor of 2 compared to the unfiltered spectrum in both cases.

The intensity of the different ZPLs is measured as a function of the angle of the detected polarization for G-0 and G-1 centers in Figs. 5(a) and 5(b). For both centers, we

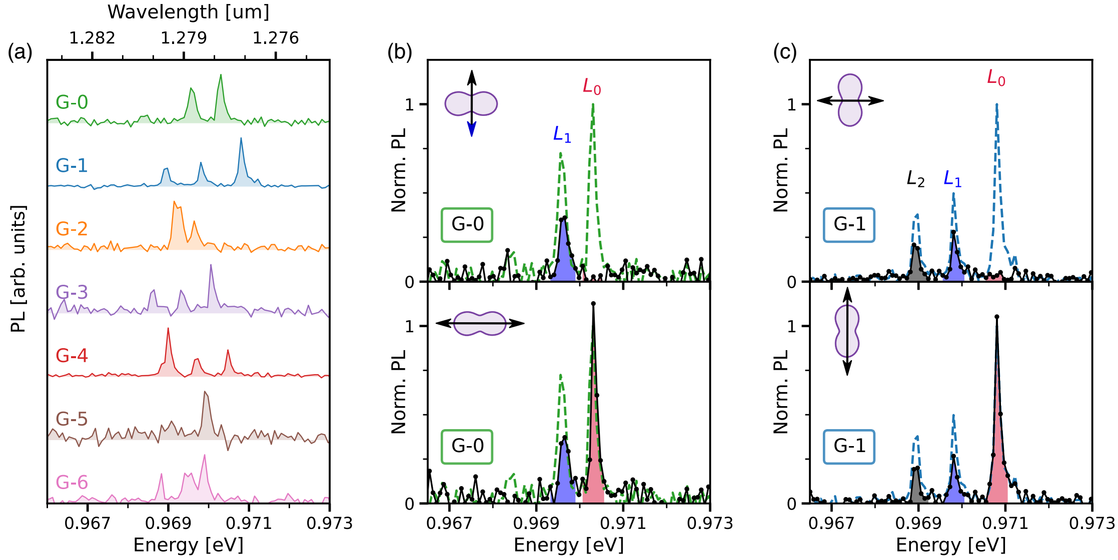

FIG. 4. Fine structure of single G centers in SOI. (a) High-resolution ZPL spectra recorded on single G centers. (b)[(c)] From top to bottom, ZPL spectrum measured on the defect G-0 [G-1] while filtering on the polarization perpendicular and parallel to the main axis of the defect polarization diagram, respectively, as indicated in the top left corners. Note that the orientation of these two defects in the crystal is different: $[\bar{1}11]$ or $[1\bar{1}1]$ for G-0 and $[111]$ or $[\bar{1}\bar{1}1]$ for G-1. The spectra with no polarization filtering from (a) are reproduced in dashed lines; the other PL spectra are normalized to its maximum. Colored areas represent the 0.3-meV integration range used in Figs. 5(a) and 5(b).

observe that the L_0 line is linearly polarized as its intensity follows a sinusoidal modulation with a visibility close to unity: $90 \pm 10\%$ and $94 \pm 5\%$ for G-0 and G-1, respectively. In contrast, the intensity of the other lines stays globally constant as a function of polarization angle. Furthermore, the intensity ratios when the L_0 line is at maximum are roughly 2∶1 and 4∶1∶1, for G-0 and G-1, respectively.

B. Interpretation

The ZPL pattern evolution with polarization shows that the G defect environment lifts the quasidegeneracy between the optical transitions associated with the three dipole orientations of the unperturbed case. The L_0 signal variation is not compatible with the emission from three dipoles described above and results instead from a single dipole. Since the L_0 intensity reaches a maximum at 0° for G-0 [90° for G-1], we can associate it to the [110] dipole ($[1\bar{1}0]$ dipole for G-1). According to Fig. 3(f), such an emission can take place only if the $\mathrm{Si}_{(\mathrm{i})}$ is localized in one of the two interstitial sites 0 or 3 [Figs. 5(a) and 5(b)]. Considering the emission dipoles allowed by the symmetry of the G center (see Sec. IV), to produce the L_1 and L_2 lines, the only possible explanation is an equal mixture of dipoles [101] and [011] for the center G-0 (dipoles $[\bar{1}01]$ and $[01\bar{1}]$ for G-1). For the G-0 doublet, this implies that the L_1 line corresponds to the four positions $\{1, 2, 4, 5\}$ of the interstitial silicon atom [Figs. 3(e) and 5(a)]. Assuming that all $\mathrm{Si}_{(\mathrm{i})}$ sites are equally occupied over the time of the acquisition, the relative intensity of L_1 after the polarizer should be $\simeq 1/2.1$ of the maximum intensity of L_0 according to FDTD simulations (Appendix A). Within error bars, these values well match the experimental data for G-0 displaying maximal intensity ratio of 2∶1, as shown in Fig. 5(a). Following the same reasoning for defect G-1, possible $\mathrm{Si}_{(\mathrm{i})}$ position configurations for the lines L_2 and L_1 would be $\{1, 2\}$ and $\{4, 5\}$ or $\{1, 5\}$ and $\{2, 4\}$ [Fig. 5(b)]. Furthermore, their relative intensity should be half that of the line L_1 of G-0 associated to twice more sites. This interpretation is in good agreement with the experimental data for G-1 showing maximal intensity ratios of roughly 4∶1∶1 [Fig. 5(b)]. We note that the G-3 center that also has a triplet fine structure shows the same polarization behavior as G-1 (see Appendix B). It is, therefore, very likely that these two defects experience a similar perturbation at first order.

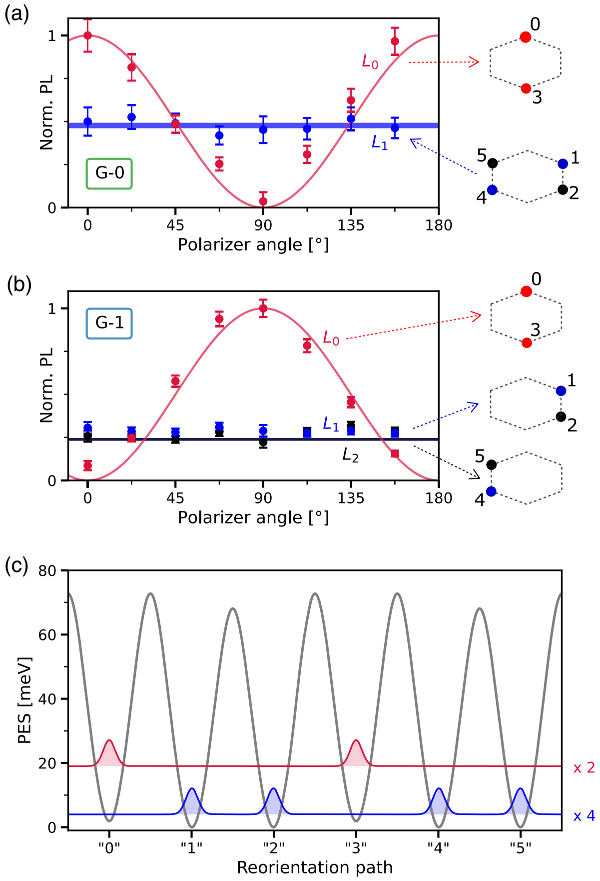

FIG. 5. Signature of the localization of $\mathrm{Si}_{(\mathrm{i})}$ in single G centers. (a),(b) Evolution of the ZPL intensity vs angle of the detected polarization for defects G-0 and G-1, respectively [see Figs. 4(b) and 4(c)]. Solid lines are models considering the emission lines result from the $\mathrm{Si}_{(\mathrm{i})}$ sites indicated in the hexagons on the right. (c) In gray, calculated PES along the motion path of the interstitial silicon atom for a G center in the ground state under 0.1% $[1\bar{1}0]$-uniaxial strain. In colors, numerical solutions for the resulting states with level degeneracy indicated on the right. The energy splitting is increased for clarity and should not be compared to the energy scale on the PES.

The ZPL evolution with polarization establishes that the defect center of mass is not in delocalized rotational states, as expected for unperturbed G centers (Sec. II). Instead, these G defects experience an external perturbation distorting their original symmetry and freezing the rotational dynamics of their center of mass. Partial delocalization of $\mathrm{Si}_{(\mathrm{i})}$ could still happen between adjacent sites (i.e., for $\{1, 2\}$ or $\{4, 5\}$) but only if their energy difference is on the order of or smaller than the tunneling coupling energy. Given the energy scale at stake here compared to $\delta_{0,\mathrm{ES}} \simeq 2.5\ \mu\mathrm{eV}$ (see Sec. II), we can consider this tunneling effect to be unlikely for the single G centers under study. Consequently, the center-of-mass eigenstates in both ground and excited states are the wave functions localized on each of the six $\mathrm{Si}_{(\mathrm{i})}$ sites and not the Bloch states derived previously in Sec. II.

Let us introduce $\tilde{E}_{\mathrm{GS}}^{(n)}$ and $\tilde{E}_{\mathrm{ES}}^{(n)}$, the defect energy when the $\mathrm{Si}_{(\mathrm{i})}$ is located in site n for the ground and excited states, respectively. The selection rules derived in the Franck-Condon approximation naturally [Eq. (6)] imply that the localized site of the defect center of mass is preserved during optical emission. As a result, the energy of the ZPL associated to the $\mathrm{Si}_{(\mathrm{i})}$ being on site n is $\tilde{E}_{\mathrm{ES}}^{(n)} - \tilde{E}_{\mathrm{GS}}^{(n)}$. Since the G center has comparable geometric configurations in the ground and excited states, the $\mathrm{Si}_{(\mathrm{i})}$ sites corresponding to degenerate ZPL transitions have also the same energy levels. For instance, for the doublet ZPL fine structure of G-0 defect, we can infer that

$$\tilde{E}_{\mathrm{GS}}^{(0)} \simeq \tilde{E}_{\mathrm{GS}}^{(3)}, \qquad \tilde{E}_{\mathrm{GS}}^{(1)} \simeq \tilde{E}_{\mathrm{GS}}^{(2)} \simeq \tilde{E}_{\mathrm{GS}}^{(4)} \simeq \tilde{E}_{\mathrm{GS}}^{(5)}. \tag{7}$$

The same relations hold as well for the excited state. The energy separation between the ZPL L_0 and L_1 is, thus, $|\tilde{\Delta}_{\mathrm{ES}} - \tilde{\Delta}_{\mathrm{GS}}|$, where $\tilde{\Delta}$ is defined as the energy splitting between the two subsets of degenerate localized states, i.e., $\tilde{\Delta} \simeq \tilde{E}^{(0)} - \tilde{E}^{(1)}$.

Although the optical transitions preserve the configuration of the defect, our observations show that the $\mathrm{Si}_{(\mathrm{i})}$ of these single G centers does move over the acquisition time. More precisely, it spends on average the same amount of time in each of the six possible sites. This motion cannot be thermally activated hopping as $k_B T$ ($\simeq$2.6 meV at 30 K) is much smaller than the potential barrier energies in both the ground and excited states (89 and 33 meV, respectively, from Ref. [15]). Instead, the motion of the center of mass of G centers could result from the excess energy provided to the system during the above-band-gap optical excitation. As this off-resonant excitation is not a direct transition, the selection rules derived for resonant optical transitions do not apply [Eq. (6)]. At each optical excitation, the interstitial silicon of the G center randomly hops between the different positions, like a ball in a six-slot casino roulette wheel. By repeating the optical cycles, each $\mathrm{Si}_{(\mathrm{i})}$ site is on average equally occupied, thus explaining our experimental data from Secs. IV and V. The next step is to determine which perturbation is responsible for preventing the delocalization dynamics of these individual G centers and generating the observed fine structures.

VI. PERTURBATIONS FROM SOI STRUCTURES

Since single G centers are incorporated in a SOI structure, the first perturbation that comes to mind is lattice strain. Indeed, the difference in thermal expansion coefficients between Si and SiO_2 leads to in-plane strain in the top silicon layer [46]. Furthermore, even state-of-the-art commercial SOI wafers are known to present lattice undulations at the micron scale resulting from the bonding process used during fabrication [47]. To test whether the ZPL splitting patterns come from the SOI structure, we first investigate G defects fabricated with a similar coimplantation method in a bulk silicon sample made of 1.5 μm of ^{28}Si on top of a natural Si substrate. G defects are created using a fluence of 10^{10} cm^{-2} for both carbon atoms and protons and with the same energies as for the SOI sample (Sec. III). Figure 6 shows the ZPL spectra measured on randomly chosen isolated G center spots in the bulk sample. For all investigated defects, a single ZPL line at 1278.6 nm is observed and without any ZPL fine structure found. These results demonstrate that the frozen delocalization of the G defect center of mass is indeed due to its formation in the SOI structure.

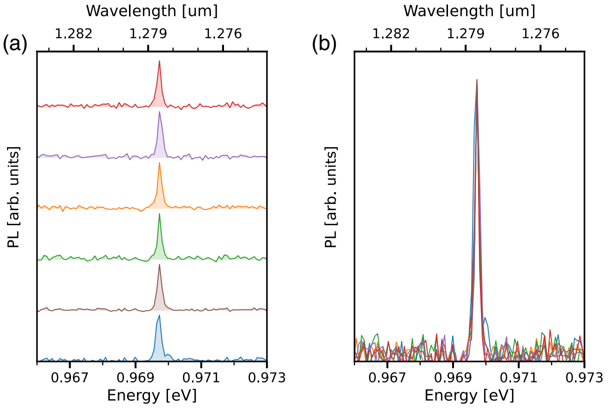

FIG. 6. ZPL spectra recorded on isolated G center spots in a bulk ^{28}Si sample plotted (a) with and (b) without vertical offset.

To evaluate the impact of homogeneous uniaxial strain on the G center, we apply DFT calculations and map the PES of the interstitial silicon atom of the defect (see Appendix C for DFT methods). As discussed in the previous section, given that the G center microscopic structure has similar geometry in both ground and excited states, the splitting pattern of the rotational levels will be qualitatively the same in both states, albeit with different energy splitting. Therefore, we can focus only on the external perturbation in the ground state.

The *ab initio* PES calculated for a G center in its ground state under 0.1% $[1\bar{1}0]$ uniaxial strain is displayed as a gray curve in Fig. 5(c). Unlike the unperturbed case from Fig. 1(c), the PES is not a sixfold symmetric periodic potential anymore. In particular, the well minima of sites 0 and 3 are shifted by $\simeq$1.9 meV compared to the four other sites [Fig. 5(c)]. Solving the time-independent Schrödinger equation for this perturbed potential leads to two separated subsets of rotational states, as shown in Fig. 5(c). The highest energy sublevel corresponds to the two degenerate states localized on sites 0 and 3, whereas the lowest one is associated to the four degenerate states localized on sites $\{1, 2, 4, 5\}$. Consequently, such $[1\bar{1}0]$ uniaxial strain does freeze the delocalization of the $\mathrm{Si}_{(\mathrm{i})}$ of the G center. Furthermore, as optical transitions occur between states localized at the same PES potential minima, this strain perturbation explains the doublet fine structure observed on G-0 defect [Fig. 5(a)]. Our calculations indicate that the origin of the ZPL splitting pattern is the energy difference of the center-of-mass potential minima between the excited and ground states.

To explain the G center triplet fine structure, an extra perturbation needs to be added to the uniaxial strain to split the fourfold sublevel [Fig. 5(b)]. A possible candidate could be an electric field, possibly coming from localized charges at the silicon-to-oxide interface [48]. The impact of an electric field on G centers is beyond the scope of the paper and will be investigated in future works.

At last, to compare different uniaxial strain directions, the ZPL energies are estimated using the Delta self-consistent-field (ΔSCF) method described in Ref. [49], for each set of equivalent equilibrium frozen configurations of the G center. The ΔSCF method is used here, as calculating the PES for each strain direction and magnitude would be too heavy on computational resources. As shown in Appendix C, for the four simulated strain directions, namely, $[1\bar{1}0]$, [110], [001], and [111], only the magnitude of the ZPL splitting and the overall energy shift of the spectrum differ between different directions. Especially, hardly any splitting is observed for the [111] strain, because this totally symmetric perturbation equally modifies the barrier energy for all sites at first order. Assuming a linear strain regime, this calculation method qualitatively reproduces the ZPL splittings observed on ensembles of G centers under uniaxial stress along (001), (111), and (110) [35] (see Appendix C). This confirms its validity for estimating the behavior of the G center ZPL doublet with strain direction.

VII. CONCLUSION

In this work, we have investigated the center-of-mass motion of the G center in silicon resulting from the motion of its intrinsic interstitial silicon atom between six crystal sites. For the unperturbed G center, the distinctive quartet fine structure arising from the $\mathrm{Si}_{(\mathrm{i})}$ perfect delocalization by tunnel effect and the subsequent selection rules for the optical transitions can be derived from a simple tight-binding model. Single-photon polarization analysis from individual defects shows that the G center emission emanates from three dipoles matching the six possible sites of the $\mathrm{Si}_{(\mathrm{i})}$. Individual G centers in ^{28}SOI exhibit ZPL fine structures that strongly vary not only from one center to another, but above all with approximately 1-meV energy splittings. Such ZPL splittings are more than 2 orders of magnitude larger than the one observed on an ensemble of unperturbed G centers in bulk ^{28}Si [2]. The evolution of the ZPL patterns with polarization evidences that the optical transitions of these single G centers are not compatible with a center-of-mass delocalization and instead occur while the $\mathrm{Si}_{(\mathrm{i})}$ sits at a fixed position, chosen among the six potential minima. *Ab initio* simulations identify uniaxial strain as being the dominant mechanism blocking the G center tunneling rotation by partially lifting the energy degeneracy between the different $\mathrm{Si}_{(\mathrm{i})}$ sites. The correlation between the strain inherent to the SOI structure and the giant ZPL fine structure measured on single G centers is corroborated by the lack of any ZPL splitting for G centers fabricated with the same ion implantation method but in a ^{28}Si bulk sample. As above-band-gap excitation does not obey the selection rules for direct optical transitions, we believe this off-resonant excitation causes the $\mathrm{Si}_{(\mathrm{i})}$ to hop randomly between the six sites, as if it were shaken in a six-slot roulette wheel.

The current results are a milestone on the road to controlling the quantum properties of the G center in silicon. The sensitivity of its fine structure to lattice distortion could be used as submicron-scale optical strain sensor in SOI-based nanomechanical resonators [50]. Furthermore, strain tuning of the defect optical emission wavelengths could be an alternative pathway to standard electrical tuning based on the Stark effect [51,52]. As the motion of the $\mathrm{Si}_{(\mathrm{i})}$ is also allowed in the metastable electron spin triplet level [15,34,39,53], investigating the rotational dynamics of the G center could also be performed through its spin quantum degree of freedom.

Our results highlight the key role on the properties of color centers of the inhomogeneous strain field in SOI films. The resulting ZPL fluctuations between defects, as shown here for G centers, will have to be efficiently compensated in view of developing quantum photonic chips relying on the emission from multiple color centers. However, far from being only a drawback, strain perturbation looks to be an attractive resource in the specific case of the G center, as it enables one to isolate single-dipole optical transitions following the freezing of its center-of-mass delocalization. This opens the route toward an efficient coupling to single-mode SOI nanophotonic cavities for cavity quantum electrodynamics experiments. For instance, in contrast, Purcell-enhanced PL will be reduced for the unpolarized optical transitions of unperturbed G centers [54]. In this context, it is worth mentioning that suspended silicon nanobeams fabricated by selectively etching the buried silica are likely to remove the microscale strain fluctuations resulting from the Si-SiO_2 interface in order for the G centers to experience the same unperturbed strainless environment [47]. Following local strain engineering strategies developed for the tuning of semiconductor laser emission [55,56], these nanostructures could also be combined with adjacent tensor arms to provide a homogeneous strain environment for color centers. As a result, the G centers will exhibit highly uniform optical emission lines with no center-of-mass delocalization. Taking benefit of these recent advances, one could use strain to engineer the PL properties of G centers in silicon in a deterministic way.

ACKNOWLEDGMENTS

We acknowledge funding from the French National Research Agency (ANR) through the projects OCTOPUS (No. ANR-18-CE47-0013-01) and QUASSIC (No. ANR-18-ERC2-0005-01), the Plan France 2030 through the project OQuLuS ANR-22-PETQ-0013, the Occitanie region through the SITEQ contract, and the European Research Council (ERC) under the European

Union's Horizon 2020 research and innovation program (project SILEQS, Grant No. 101042075). A. Durand acknowledges support from the French DGA. A. G. acknowledges the support by the Ministry of Culture and Innovation and the National Research, Development and Innovation Office within the Quantum Information National Laboratory of Hungary (Grant No. 2022-2.1.1-NL-2022-00004). A. G. additionally acknowledges the high-performance computational resources provided by KIFÜ (Governmental Agency for IT Development) institute of Hungary and the European Commission for project QuMicro (Grant No. 101046911). The authors thank François Rieutord for enlightening discussions regarding lattice strain in SOI wafers.

APPENDIX A: DIPOLE COLLECTION EFFICIENCIES

In solid-state systems, the properties of light emitters vary depending on their local environment. For a point emitter embedded within a thin dielectric film (such as G centers in our experiments), both the spontaneous emission rate and the radiation diagram are strongly modified with respect to the ones it would exhibit in a uniform dielectric medium. They furthermore depend on the orientation of the emitter's optical dipole as well as its distance to the film interfaces [57,58]. These effects can be accurately simulated numerically using the FDTD method [43]. We implement in the present work the commercial software suite RSOFT from Synopsys (version 19.09). Since the top surface of the SOI sample is (001) oriented, both $[\bar{1}01]$ and $[01\bar{1}]$ dipoles will lead to the same results [see Fig. 3(e)]. The dipole spontaneous emission enhancement factor F resulting from Purcell effect in the top silicon layer is computed as function of the defect depth for $[1\bar{1}0]$ and $[01\bar{1}]$ dipoles [Fig. 7(a)]. The value of F indicates whether the dipole emission is enhanced ($F > 1$) or reduced ($F < 1$) compared to its value in bulk silicon. While the emission of the $[1\bar{1}0]$ in-plane dipole is little affected, the one of the $[01\bar{1}]$ out-of-plane dipole is inhibited by a factor of $\simeq 2$ due to the SOI structure. On the contrary, the dipole orientation has a small impact on its collection efficiency C_{eff} through a 0.85-numerical aperture microscope objective, as shown in Fig. 7(b). However, it strongly varies with the dipole depth, from $\simeq 2.5\%$ at the surface to $\simeq 4.5\%$ at the oxide interface. The total collected PL is proportional to the product $F \cdot C_{\mathrm{eff}}$ for each dipole [Fig. 7(c)]. As its relaxation is strongly dominated by nonradiated decay channels [24], we implicitly assume that the excitation probability of the G center is not impacted by the Purcell effect. To obtain the relative contribution between the in-plane and out-of-plane dipoles, we compute the ratio $r = (F^{[1\bar{1}0]} \cdot C_{\mathrm{eff}}^{[1\bar{1}0]})/(F^{[01\bar{1}]} \cdot C_{\mathrm{eff}}^{[01\bar{1}]})$. As displayed in Fig. 7(d), the defect depth has little influence on this ratio that evolves in the [2.0–2.2] range within the 60-nm-thick silicon layer.

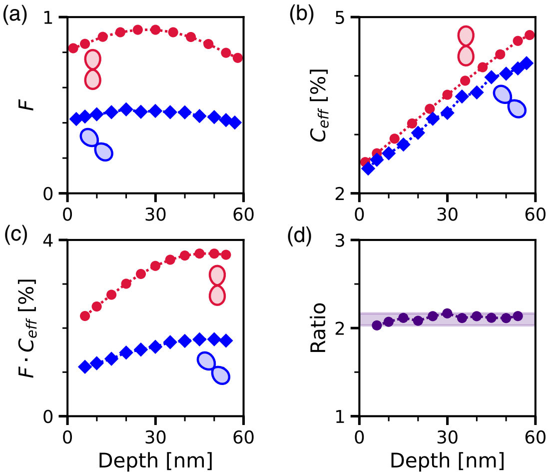

FIG. 7. Numerical simulations using the FDTD method of the dipole collected intensity as a function of the defect depth. (a)–(c) Respectively, Purcell factor F, collection efficiency C_{eff}, and their product for the dipoles $[1\bar{1}0]$ (red) and $[01\bar{1}]$ (blue). (d) Evolution of the relative PL contribution between these two dipoles.

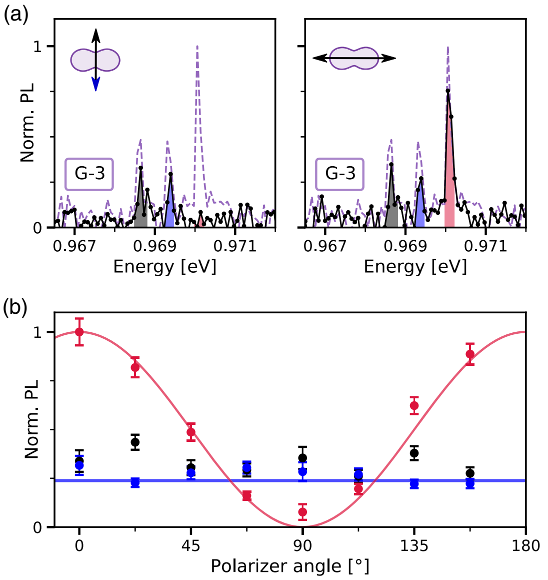

FIG. 8. Triplet ZPL fine structure of G-3 defect. (a) From left to right, ZPL spectrum measured on the defect G-3 with a polarizer selecting the polarization perpendicular and parallel to the main axis of the defect polarization diagram, respectively, as indicated in the top left corners. The spectra with no polarization filtering from Fig. 4(a) are reproduced in dashed lines; the y axis is normalized to its maximum. Colored areas represent the 0.2-meV integration range used in (b). (b) Evolution of the intensity of the three ZPLs vs angle of the detected polarization [see Figs. 4(b) and 4(c)]. Solid lines are models considering the emission lines result from the $\mathrm{Si}_{(\mathrm{i})}$ sites indicated in Fig. 4(b).

APPENDIX B: TRIPLET FINE STRUCTURE ANALYSIS ON DEFECT G-3

The spectral analysis with polarization from Sec. V is performed on the single G center G-3 that presents a triplet ZPL fine structure. The evolution of its ZPL with polarization filtering reproduces the behavior observed on the triplet fine structure of defect G-1 [Figs. 4(c) and 5(b)]. Especially, we measure again that the highest optical line is fully canceled for polarization perpendicular to the defect emission diagram [Fig. 8(a)]. The quantitative analysis of the ZPL intensities as a function of detected polarization angle shows that this line is indeed linearly polarized while the other two ZPLs are unpolarized [Fig. 8(b)], as circularly polarized photons are not compatible with the symmetry of the G center (see Sec. IV). Like the single G centers in SOI previously investigated, the PL from the G-3 defect results from optical transitions occurring between localized states of its center of mass. In particular, the ZPL fine structure of the G-3 center could be explained by the same localized $Si_{(i)}$ sites as for the G-1 center, such as the ones proposed in Fig. 5(b).

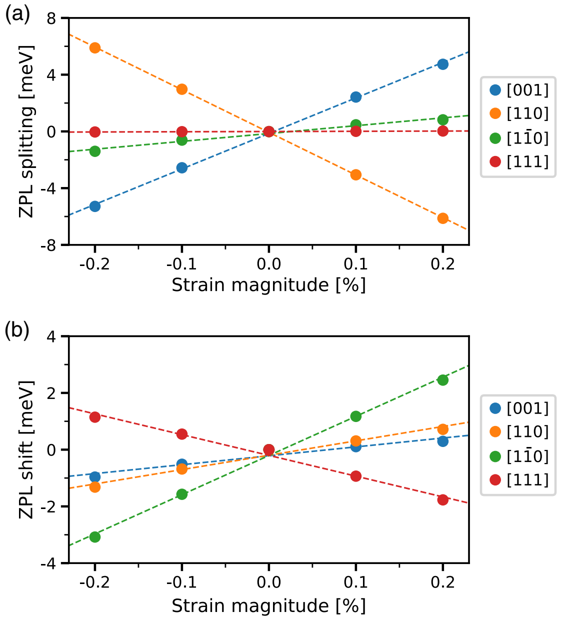

FIG. 9. Energy of the (a) ZPL doublet splitting and (b) average ZPL shift for a [111]-oriented G center under various directions of uniaxial strain, calculated using the ΔSCF method.

APPENDIX C: *AB INITIO* CALCULATIONS FOR PERTURBED G CENTERS

1. DFT methods

We apply DFT calculations on a G center perturbed by uniaxial strain and map the ground state PES along the rotational motion path of the central silicon atom of the G center. Along the associated Q vibrational coordinate, we sample all six minima and barrier points and one additional middle point between these, using 24 single-point calculations in total for a single PES calculation. These geometric configurations are relaxed by climbing image nudged elastic band method on the sampling images until a 10^{-4}eV/Å threshold is reached in the forces. This precision is necessary for the accurate modeling of small perturbations resulting in small relative energy differences. Consequently, we need to compromise the accuracy in the total energy by using the Perdew-Burke-Ernzerhof functional. The calculations are performed in the plane-wave-based Vienna *Ab initio* Simulation Package (VASP) [59]. The defect is modeled in a large 512-atom supercell with single Γ-point sampling in the reciprocal space. The core electrons are treated in the projector augmented wave formalism [60–63]. The atomic positions remain fixed

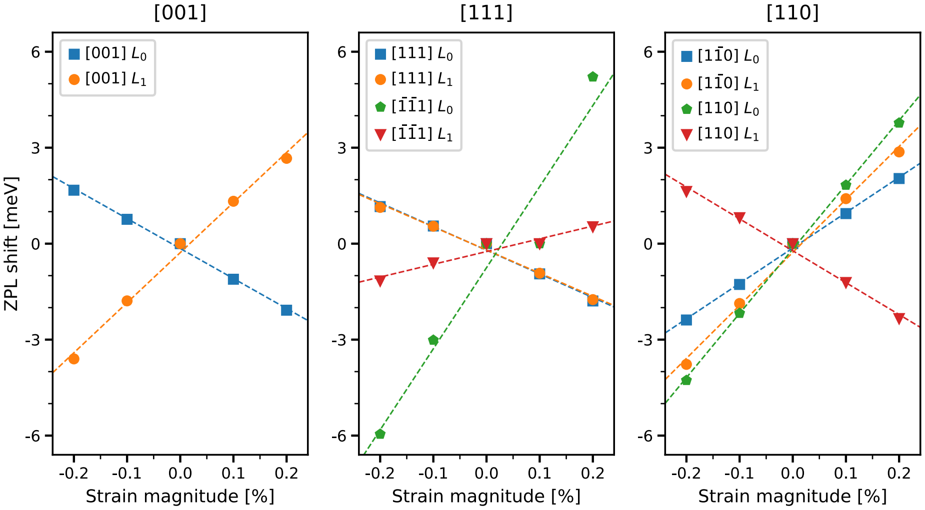

FIG. 10. Evolution of the energy shift of the two ZPLs L_0 and L_1 of a [111]-oriented G defect under different uniaxial strain directions to mimic the behavior of an ensemble of G centers under [001], [111], and [110] uniaxial strain, respectively. Numerical simulations were performed using the ΔSCF method.

during this calculation. The rotational reorientation is modeled in analogy to our previous work in Ref. [15].

2. ZPL patterns for different uniaxial strains

We estimate the evolution of the ZPL patterns under different strain directions using the ΔSCF method in the nonequivalent local minima positions. We can safely assume that the ZPL shift is dominated by the relative energy shift in the local minima of the PES for the larger strain regimes where frozen position approximation holds. We note that this simulation method is not accurate to predict the correct ZPL energy ($\simeq$654 meV for the unperturbed G center), but it enables one to qualitatively extract strain-induced ZPL splitting trends, as shown in the following. The ZPL energy is calculated for each subset of equivalent equilibrium $\mathrm{Si}_{(\mathrm{i})}$ positions for four uniaxial strain directions: [001], [110], $[1\bar{1}0]$, and [111]. As visible in Fig. 9(a), the ZPL splitting energies are proportional to the strain amplitude in the $[-0.2\%, +0.2\%]$ investigated range. The largest splitting is obtained for the [110] strain, while hardly any splitting is observed for the [111] strain, as it corresponds to a totally symmetric perturbation. All four simulated strain directions produce an overall shift of the ZPL doublet fine structure [Fig. 9(b)].

As a safety check, we calculate the evolution of the ZPL patterns of an ensemble of G centers subject to uniaxial strain along the crystal directions used in a previous piezospectroscopic experiment [35] (Fig. 10). For a [001] strain, all four possible $\langle 111\rangle$ crystal axes of the G center experience the same lattice distortion and, hence, the same doublet fine structure. Under a [111] strain, the [111]-oriented G centers will feel a totally symmetric perturbation with no splitting, while the three other G orientations will undergo a perturbation equivalent to a $[\bar{1}\bar{1}1]$ strain for [111]-oriented G center. Consequently, three optical lines are expected to split for a G-center ensemble under [111] strain. The [110] strain will separate the orientations into two families: [111]- and $[\bar{1}\bar{1}1]$-oriented centers, on one hand, and $[\bar{1}11]$- and $[1\bar{1}1]$-oriented defects, on the other hand. The strain experienced by these last two orientations will be equivalent to a $[1\bar{1}0]$ strain acting on a [111]-oriented G center. As a result, four optical lines are expected to emerge for an ensemble of G defects under [110]-uniaxial strain. Assuming the linear regime of Hooke's law prevails, the ZPL splittings calculated for these three uniaxial strains are in good qualitative agreement with the uniaxial stress measurements performed on a ensemble of G centers in Ref. [35].

[1] C. Beaufils, W. Redjem, E. Rousseau, V. Jacques, A. Y. Kuznetsov, C. Raynaud, C. Voisin, A. Benali, T. Herzig, S. Pezzagna, J. Meijer, M. Abbarchi, and G. Cassabois, *Optical properties of an ensemble of G-centers in silicon*, Phys. Rev. B **97**, 035303 (2018).

[2] C. Chartrand, L. Bergeron, K. J. Morse, H. Riemann, N. V. Abrosimov, P. Becker, H.-J. Pohl, S. Simmons, and M. L. W. Thewalt, *Highly enriched* ^{28}Si *reveals remarkable optical linewidths and fine structure for well-known damage centers*, Phys. Rev. B **98**, 195201 (2018).

[3] W. Redjem, A. Durand, T. Herzig, A. Benali, S. Pezzagna, J. Meijer, A. Yu. Kuznetsov, H. S. Nguyen, S. Cueff, J.-M. Gérard, I. Robert-Philip, B. Gil, D. Caliste, P. Pochet, M. Abbarchi, V. Jacques, A. Dréau, and G. Cassabois, *Single artificial atoms in silicon emitting at telecom wavelengths*, Nat. Electron. **3**, 738 (2020).

[4] S. Simmons, *A single silicon colour centre resolved*, Nat. Electron. **3**, 734 (2020).

[5] M. Hollenbach, Y. Berencén, U. Kentsch, M. Helm, and G. V. Astakhov, *Engineering telecom single-photon emitters in silicon for scalable quantum photonics*, Opt. Express **28**, 26111 (2020).

[6] G. Zhang, Y. Cheng, J.-P. Chou, and A. Gali, *Material platforms for defect qubits and single-photon emitters*, Appl. Phys. Rev. **7**, 031308 (2020).

[7] A. Durand, Y. Baron, W. Redjem, T. Herzig, A. Benali, S. Pezzagna, J. Meijer, A. Y. Kuznetsov, J.-M. Gérard, I. Robert-Philip, M. Abbarchi, V. Jacques, G. Cassabois, and A. Dréau, *Broad diversity of near-infrared single-photon emitters in silicon*, Phys. Rev. Lett. **126**, 083602 (2021).

[8] L. Bergeron, C. Chartrand, A. T. K. Kurkjian, K. J. Morse, H. Riemann, N. V. Abrosimov, P. Becker, H.-J. Pohl, M. L. W. Thewalt, and S. Simmons, *Silicon-integrated telecommunications photon-spin interface*, PRX Quantum **1**, 020301 (2020).

[9] D. B. Higginbottom, A. T. K. Kurkjian, C. Chartrand, M. Kazemi, N. A. Brunelle, E. R. MacQuarrie, J. R. Klein, N. R. Lee-Hone, J. Stacho, M. Ruether, C. Bowness, L. Bergeron, A. DeAbreu, S. R. Harrigan, J. Kanaganayagam, D. W. Marsden, T. S. Richards, L. A. Stott, S. Roorda, K. J. Morse, M. L. W. Thewalt, and S. Simmons, *Optical observation of single spins in silicon*, Nature (London) **607**, 266 (2022).

[10] D. B. Higginbottom, F. K. Asadi, C. Chartrand, J.-W. Ji, L. Bergeron, M. L. W. Thewalt, C. Simon, and S. Simmons, *Memory and transduction prospects for silicon T center devices*, PRX Quantum **4**, 020308 (2023).

[11] A. DeAbreu, C. Bowness, A. Alizadeh, C. Chartrand, N. A. Brunelle, E. R. MacQuarrie, N. R. Lee-Hone, M. Ruether, M. Kazemi, A. T. K. Kurkjian, S. Roorda, N. V. Abrosimov, H.-J. Pohl, M. L. W. Thewalt, D. B. Higginbottom, and S. Simmons, *Waveguide-integrated silicon T centres*, Opt. Express **31**, 15045 (2023).

[12] A. Johnston, U. Felix-Rendon, Y.-E. Wong, and S. Chen, *Cavity-coupled telecom atomic source in silicon*, Nat. Commun. **15**, 2350 (2024).

[13] C.-M. Lee, F. Islam, S. Harper, M. A. Buyukkaya, D. Higginbottom, S. Simmons, and E. Waks, *High-efficiency single photon emission from a silicon T-center in a nanobeam*, ACS Photonics **10**, 3844 (2023).

[14] F. Islam, C.-M. Lee, S. Harper, M. H. Rahaman, Y. Zhao, N. K. Vij, and E. Waks, *Cavity-enhanced emission from a silicon T center*, Nano Lett. **24**, 319 (2024).

[15] P. Udvarhelyi, B. Somogyi, G. Thiering, and A. Gali, *Identification of a telecom wavelength single photon emitter in silicon*, Phys. Rev. Lett. **127**, 196402 (2021).

[16] Y. Baron, A. Durand, T. Herzig, M. Khoury, S. Pezzagna, J. Meijer, I. Robert-Philip, M. Abbarchi, J.-M. Hartmann, S. Reboh, J.-M. Gérard, V. Jacques, G. Cassabois, and A. Dréau, *Single G centers in silicon fabricated by co-implantation with carbon and proton*, Appl. Phys. Lett. **121**, 084003 (2022).

[17] M. Hollenbach, N. Klingner, N. S. Jagtap, L. Bischoff, C. Fowley, U. Kentsch, G. Hlawacek, A. Erbe, N. V. Abrosimov, M. Helm, Y. Berencén, and G. V. Astakhov, *Wafer-scale nanofabrication of telecom single-photon emitters in silicon*, Nat. Commun. **13**, 7683 (2022).

[18] L. Komza, P. Samutpraphoot, M. Odeh, Y.-L. Tang, M. Mathew, J. Chang, H. Song, M.-K. Kim, Y. Xiong, G. Hautier, and A. Sipahigil, *Indistinguishable photons from an artificial atom in silicon photonics*, Nat. Commun. **15**, 6920 (2024).

[19] B. Lefaucher, J.-B. Jager, V. Calvo, A. Durand, Y. Baron, F. Cache, V. Jacques, I. Robert-Philip, G. Cassabois, T. Herzig, J. Meijer, S. Pezzagna, M. Khoury, M. Abbarchi, A. Dréau, and J.-M. Gérard, *Cavity-enhanced zero-phonon emission from an ensemble of G centers in a silicon-on-insulator microring*, Appl. Phys. Lett. **122**, 061109 (2023).

[20] M. Prabhu, C. Errando-Herranz, L. De Santis, I. Christen, C. Chen, C. Gerlach, and D. Englund, *Individually addressable and spectrally programmable artificial atoms in silicon photonics*, Nat. Commun. **14**, 2380 (2023).

[21] V. Saggio, C. Errando-Herranz, S. Gyger, C. Panuski, M. Prabhu, L. De Santis, I. Christen, D. Ornelas-Huerta, H. Raniwala, C. Gerlach, M. Colangelo, and D. Englund, *Cavity-enhanced single artificial atoms in silicon*, Nat. Commun. **15**, 5296 (2024).

[22] A. M. Day, M. Sutula, J. R. Dietz, A. Raun, D. D. Sukachev, M. K. Bhaskar, and E. L. Hu, *Electrical manipulation of telecom color centers in silicon*, Nat. Commun. **15**, 4722 (2024).

[23] K. Jhuria, V. Ivanov, D. Polley, Y. Zhiyenbayev, W. Liu, A. Persaud, W. Redjem, W. Qarony, P. Parajuli, Q. Ji, A. J. Gonsalves, J. Bokor, L. Z. Tan, B. Kanté, and T. Schenkel, *Programmable quantum emitter formation in silicon*, Nat. Commun. **15**, 4497 (2024).

[24] A. Durand, Y. Baron, F. Cache, T. Herzig, M. Khoury, S. Pezzagna, J. Meijer, J.-M. Hartmann, S. Reboh, M. Abbarchi, I. Robert-Philip, J.-M. Gérard, V. Jacques, G. Cassabois, and A. Dréau, *Genuine and faux single G centers in carbon-implanted silicon*, Phys. Rev. B **110**, L020102 (2024).

[25] J. Aberl, E. P. Navarrete, M. Karaman, D. H. Enriquez, C. Wilflingseder, A. Salomon, D. Primetzhofer, M. A. Schubert, G. Capellini, T. Fromherz, P. Deák, P. Udvarhelyi, S.Li, A. Gali, and M. Brehm, *All-epitaxial self-assembly of silicon color centers confined within sub-nanometer thin layers using ultra-low temperature epitaxy*, Adv. Mater. **36**, 2408424 (2024).

[26] I. R. Berkman, A. Lyasota, G. G. de Boo, J. G. Bartholomew, S. Q. Lim, B. C. Johnson, J. C. McCallum, B.-B. Xu, S. Xie, N. V. Abrosimov, H.-J. Pohl, R. L. Ahlefeldt, M. J. Sellars, C. Yin, and S. Rogge, *Millisecond electron spin coherence time for erbium ions in silicon*, arXiv:2307.10021.

[27] L. Weiss, A. Gritsch, B. Merkel, and A. Reiserer, *Erbium dopants in nanophotonic silicon waveguides*, Optica **8**, 40 (2021).

[28] A. Gritsch, A. Ulanowski, and A. Reiserer, *Purcell enhancement of single-photon emitters in silicon*, Optica **10**, 783 (2023).

[29] W. Redjem, Y. Zhiyenbayev, W. Qarony, V. Ivanov, C. Papapanos, W. Liu, K. Jhuria, Z. Y. Al Balushi, S. Dhuey, A. Schwartzberg, L. Z. Tan, T. Schenkel, and B. Kanté, *All-silicon quantum light source by embedding an atomic emissive center in a nanophotonic cavity*, Nat. Commun. **14**, 3321 (2023).

[30] Y. Zhiyenbayev, W. Redjem, V. Ivanov, W. Qarony, C. Papapanos, J. Simoni, W. Liu, K. Jhuria, L. Z. Tan, T. Schenkel, and B. Kanté, *Scalable manufacturing of quantum light emitters in silicon under rapid thermal annealing*, Opt. Express **31**, 8352 (2023).

[31] Y. Baron, A. Durand, P. Udvarhelyi, T. Herzig, M. Khoury, S. Pezzagna, J. Meijer, I. Robert-Philip, M. Abbarchi, J.-M. Hartmann, V. Mazzocchi, J.-M. Gérard, A. Gali, V. Jacques, G. Cassabois, and A. Dréau, *Detection of single W-centers in silicon*, ACS Photonics **9**, 2337 (2022).

[32] B. Lefaucher, J.-B. Jager, V. Calvo, F. Cache, A. Durand, V. Jacques, I. Robert-Philip, G. Cassabois, Y. Baron, F. Mazen, S. Kerdilès, S. Reboh, A. Dréau, and J.-M. Gérard, *Purcell enhancement of silicon W centers in circular Bragg grating cavities*, ACS Photonics **11**, 24 (2024).

[33] P. Udvarhelyi, A. Pershin, P. Deák, and A. Gali, *An L-band emitter with quantum memory in silicon*, npj Comput. Mater. **8**, 262 (2022).

[34] K. M. Lee, K. P. O'Donnell, J. Weber, B. C. Cavenett, and G. D. Watkins, *Optical detection of magnetic resonance for a deep-level defect in silicon*, Phys. Rev. Lett. **48**, 37 (1982).

[35] C. P. Foy, M. C. d. Carmo, G. Davies, and E. C. Lightowlers, *Uniaxial stress measurements on the 0.97 eV line in irradiated silicon*, J. Phys. C **14**, L7 (1981).

[36] K. Thonke, H. Klemisch, J. Weber, and R. Sauer, *New model of the irradiation-induced 0.97-eV (G) line in silicon: A* $\mathrm{C_S - Si^*}$ *complex*, Phys. Rev. B **24**, 5874 (1981).

[37] G. Davies, E. C. Lightowlers, and M. d. Carmo, *Carbon-related vibronic bands in electron-irradiated silicon*, J. Phys. C **16**, 5503 (1983).

[38] G. Davies, *The optical properties of luminescence centres in silicon*, Phys. Rep. **176**, 83 (1989).

[39] K. P. O'Donnell, K. M. Lee, and G. D. Watkins, *Origin of the 0.97 eV luminescence in irradiated silicon*, Physica (Amsterdam) **116B+C**, 258 (1983).

[40] R. B. Capaz, A. Dal Pino, and J. D. Joannopoulos, *Theory of carbon-carbon pairs in silicon*, Phys. Rev. B **58**, 9845 (1998).

[41] L. W. Song, X. D. Zhan, B. W. Benson, and G. D. Watkins, *Bistable interstitial-carbon–substitutional-carbon pair in silicon*, Phys. Rev. B **42**, 5765 (1990).

[42] C. Cohen-Tannoudji, B. Diu, and F. Laloë, *Basic Concepts, Tools, and Applications*, Quantum Mechanics Vol. 1 (Wiley, New York, 2019).

[43] A. Taflove and S. C. Hagness, *Computational Electrodynamics, the Finite-Difference Time-Domain Method*, 3rd ed. (Artech House, Boston, 2005).

[44] V. D. Tkachev and A. V. Mudryi, *Piezospectroscopic effect on zero-phonon luminescence lines of silicon*, J. Appl. Spectrosc. **29**, 1485 (1978).

[45] A. Ristori, M. Khoury, M. Salvalaglio, A. Filippatos, M. Amato, T. Herzig, J. Meijer, S. Pezzagna, D. Hannani, M. Bollani, C. Barri, C. M. Ruiz, N. Granchi, F. Intonti, M. Abbarchi, and F. Biccari, *Strain engineering of the electronic states of silicon-based quantum emitters*, Adv. Opt. Mater. **12**, 2301608 (2024).

[46] J. Camassel, L. A. Falkovsky, and N. Planes, *Strain effect in silicon-on-insulator materials: Investigation with optical phonons*, Phys. Rev. B **63**, 035309 (2000).

[47] K. Fukuda, T. Yoshida, T. Shimura, K. Yasutake, M. Umeno, and S. Iida, *White x-ray topography of lattice undulation in bonded silicon-on-insulator wafers*, Jpn. J. Appl. Phys. **45**, 6795 (2006).

[48] D. K. Schroder, *Semiconductor Material and Device Characterization*, 1st ed. (Wiley, New York, 2005).

[49] A. Gali, E. Janzén, P. Deák, G. Kresse, and E. Kaxiras, *Theory of spin-conserving excitation of the* $N - V^{-}$ *center in diamond*, Phys. Rev. Lett. **103**, 186404 (2009).

[50] H. G. Craighead, *Nanoelectromechanical systems*, Science **290**, 1532 (2000).

[51] L. C. Bassett, F. J. Heremans, C. G. Yale, B. B. Buckley, and D. D. Awschalom, *Electrical tuning of single nitrogen-vacancy center optical transitions enhanced by photoinduced fields*, Phys. Rev. Lett. **107**, 266403 (2011).

[52] C. F. de las Casas, D. J. Christle, J. Ul Hassan, T. Ohshima, N. T. Son, and D. D. Awschalom, *Stark tuning and electrical charge state control of single divacancies in silicon carbide*, Appl. Phys. Lett. **111**, 262403 (2017).

[53] L. S. Vlasenko, M. P. Vlasenko, V. N. Lomasov, and V. A. Khramtsov, *Spin-dependent effects due to triplet centers in irradiated silicon*, Sov. Phys. JETP **64**, 3 (1986), http://www.jetp.ras.ru/cgi-bin/e/index/e/64/3/p612?a=list.

[54] J.-M. Gérard, *Solid-state cavity-quantum electrodynamics with self-assembled quantum dots*, in *Single Quantum Dots: Fundamentals, Applications, and New Concepts*, Topics in Applied Physics (Springer, Berlin, 2003), pp. 269–314, 10.1007/978-3-540-39180-7_7.

[55] J. Chrétien, N. Pauc, F. Armand Pilon, M. Bertrand, Q.-M. Thai, L. Casiez, N. Bernier, H. Dansas, P. Gergaud, E. Delamadeleine, R. Khazaka, H. Sigg, J. Faist, A. Chelnokov, V. Reboud, J.-M. Hartmann, and V. Calvo, GeSn *lasers covering a wide wavelength range thanks to uniaxial tensile strain*, ACS Photonics **6**, 2462 (2019).

[56] K. Guilloy, N. Pauc, A. Gassenq, P. Gentile, S. Tardif, F. Rieutord, and V. Calvo, *Tensile strained germanium nanowires measured by photocurrent spectroscopy and x-ray microdiffraction*, Nano Lett. **15**, 2429 (2015).

[57] S. T. Ho, S. L. McCall, and R. E. Slusher, *Spontaneous emission from excitons in thin dielectric layers*, Opt. Lett. **18**, 909 (1993).

[58] H. Benisty, H. De Neve, and C. Weisbuch, *Impact of planar microcavity effects on light extraction—Part I: Basic concepts and analytical trends*, IEEE J. Quantum Electron. **34**, 1612 (1998).

[59] P. E. Blöchl, *Projector augmented-wave method*, Phys. Rev. B **50**, 17953 (1994).

[60] G. Kresse and J. Hafner, *Ab initio molecular dynamics for liquid metals*, Phys. Rev. B **47**, 558 (1993).

[61] G. Kresse and J. Furthmüller, *Efficient iterative schemes for ab initio total-energy calculations using a plane-wave basis set*, Phys. Rev. B **54**, 11169 (1996).

[62] G. Kresse and J. Furthmüller, *Efficiency of ab-initio total energy calculations for metals and semiconductors using a plane-wave basis set*, Comput. Mater. Sci. **6**, 15 (1996).

[63] J. Paier, M. Marsman, K. Hummer, G. Kresse, I. C. Gerber, and J. G. Ángyán, *Screened hybrid density functionals applied to solids*, J. Chem. Phys. **124**, 154709 (2006).